# Modification of The Field-Weakening Control Strategy for Linear Induction Motor Drives Considering The End Effect

Pegah HAMEDANI, Abbas SHOULAIE
*Electrical Engineering Department, Iran University of Science and Technology, Narmak, Tehran, Iran*
*p_hamedani@iust.ac.ir*

***Abstract*—Accurate vector control of a linear induction motor (LIM) drive is a complicated subject because of the end effect phenomenon especially in the field-weakening region. This paper concentrates on a novel field-weakening speed control strategy for LIM drive in which the end effect is taken into account. Considering the end effect, new voltage and current limits have been calculated using the Duncan's model. Accordingly, control strategies such as constant force region, partial field-weakening region, and full field-weakening region have been analytically calculated for the first time in this work. In order to improve the control characteristics of the LIM drive, Fuzzy Logic Controller (FLC) has been also implemented. Simulation results manifest the satisfactory resultants of the proposed FLC based LIM in the field-weakening region including fast response, no overshoot, negligible steady-state error, and adaptability to load changes. In addition, a new constant force pattern is introduced in this paper by which the reductions of the LIM thrust due to the end effect will be compensated and thus, the current and voltage amplitudes in steady state will remarkably decrease.**

***Index Terms*—field-weakening control, fuzzy logic control, linear induction motor, variable speed drives, vector control.**

## I. INTRODUCTION

Nowadays, high performance Linear Induction Motor (LIM) drives are widely used in many industrial applications, especially in transportation, due to the specific advantages they have. Therefore, accurate modeling of the LIM, which can be directly used in vector control applications, has become an indispensable challenge for the researches. The simplest method to analyze an LIM is using an equivalent circuit model. Nevertheless, equivalent circuit modeling of an LIM is not as simple as a rotary motor due to the existence of the end effect. One of the well-known per-phase equivalent circuit models of the LIM was suggested by Duncan [1]. In this model the magnetizing branch of the equivalent circuit of the rotary induction motor (RIM) was modified and the proper coefficient for reflecting the end effect was taken into account. The magnetizing inductance was modified by a coefficient reverse to the speed [1]. In addition, a series resistance appeared in the magnetizing branch reflecting the eddy current losses caused by the end effect [1]. This model was simple and useful for evaluation on the LIM characteristics, but it was not directly appropriate for vector control and drive applications. In [2] the q-d dynamic equivalent circuit model of the three-phase LIM with the end effect consideration was proposed. The authors suggested a q-d equivalent circuit model for three-phase LIM according to the Duncan's per-phase model with the end effect included. Although this model was proper for the vector control of the three-phase LIM, the end effect was only considered in the d-axis equivalent circuit. The q-axis equivalent circuit of the LIM was identical to that of an RIM and was not affected by the end effect. However, it is clear that for accurate and correct modeling of an LIM, the end effect must be considered in both q and d axes. For years, this work was the main reference in q-d dynamic modeling and vector control of three-phase LIMs with considering the end effect [3-5]. In 2005, the second author of [2] developed a new q-d dynamic model for three-phase LIM and corrected his previous work by considering the end effect for both d and q axes in the equivalent circuit [6]. This model was derived by transforming the Duncan's per-phase model into a synchronous reference frame aligned with the secondary flux using park's transformation. For the sake of simplicity, the series resistance in the magnetizing branch due to the eddy current losses was neglected in this model. In [7] the dynamic modeling of multiphase linear induction motors considering the end effect was proposed (for three or more than three phases).

On the other hand, in the area of control techniques of the LIM, beneficial investigations have been performed until now [2-7]. Indirect Field Oriented Control (IFOC) technique is one of the popular control techniques widely applied to linear induction motor drive applications [4-7]. The main idea behind IFOC in an LIM is the decoupling of the flux and the torque. The flux orientation can be achieved by aligning the secondary flux vector with the d-axis. This can be performed by keeping the d-axis secondary flux constant and setting the q-axis secondary flux to zero [4-7].

Furthermore, in many speed control applications such as spindle, traction, and electric vehicle drives, the electrical drive must deliver a constant power at high speeds [8-14]. In such cases, the Field-Weakening (FW) control strategy is a suitable control approach in which the motor flux is properly reduced as the motor speed increases [8], [13-14].

Moreover, in high-speed applications, the maximum output torque and power developed by the machine are dependent on the inverter voltage rating and the allowable current of the inverter [8], [11]. Consequently, in the field-weakening region, the motor flux should be suitably weakened, while satisfying the voltage and current constraints, which leads to economic rating of the inverter and the motor [13-14]. In the past decades, remarkable works have been reported in the literature on the FW control of the induction motor drives [8-17]. In the conventional

Digital Object Identifier 10.4316/AECE.2015.03001

FW method the rotor flux command is adjusted inversely proportional to the motor speed ($1/\omega_r$ method) [8-9], [13-14]. Nevertheless, in this method, the voltage limit cannot be fully satisfied and thus the maximum torque capability cannot be achieved [8-9], [13-14]. To solve this problem and in order to achieve maximum torque capability in the whole FW region by taking into account the current and voltage limits, various efforts have been reported [8-16]. Accordingly, the appropriate indirect field oriented control scheme is introduced in the field-weakening region.

Although the field-weakening control of the rotational induction machines has received significant attentions over the past few decades, however, in case of linear induction machines, which are widely used in many industrial applications, especially in high-speed transportation, few works has been reported in the literature. Motivated by the above discussion, an attempt is made in this paper to provide a survey in field-weakening speed control of LIMs considering the end effect. Due to the end effect phenomenon, the FW strategy in linear induction motor drives will become more complicated and the vector control should be correspondingly modified. In addition, Fuzzy Logic Controller (FLC) has been utilized in order to attain perfect control characteristics.

## II. Dynamic Modeling of The Linear Induction Motor Considering The End Effect

Fig. 1 represents the per-phase equivalent circuit model of an LIM. Duncan introduced a dimensionless factor *Q*, which is defined by [1], [18-19]:

$$Q \cong \frac{T_v}{T_r} = \frac{D.R'_r}{L'_r.v_r} \tag{1}$$

where $D$, $v_r$, $L'_r$, and $R'_r$ are the motor length, velocity, secondary self-inductance and secondary resistance, respectively [1]. $T_r = L'_r / R'_r$ is the time constant of the secondary circuit and $T_v$ is the time for the primary core to traverse a point in the rail. For the end effect inclusion in Duncan's model, the magnetizing inductance is modified to $L_{m_o}(1-f(Q))$, where $L_{m_o}$ is the magnetizing inductance at zero speed and $f(Q)=\left(1-e^{-Q}\right)/Q$ [1]. In traditional Duncan's model, a series resistance exists in the magnetizing branch which shows the eddy current losses caused by the end effect and is equal to $R'_r.f(Q)$ [1],[19]. For the sake of simplicity, this resistance is neglected in this work [6].

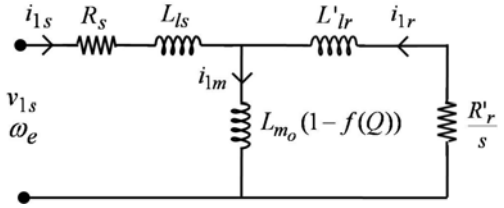


Figure 1. The per-phase equivalent circuit model of LIM

Using the Park's transformation, the n-phase LIM model in the rotational reference frame can be expressed with the following voltage and flux linkage equilibriums ($p \equiv d/dt$) [7]:

Primary voltage equations:

$$v_{qs} = R_s i_{qs} + \omega\lambda_{ds} + p\lambda_{qs}$$
$$v_{ds} = R_s i_{ds} - \omega\lambda_{qs} + p\lambda_{ds} \tag{2}$$

Secondary voltage equations:

$$v_{qr} = R'_r i_{qr} + (\omega - \omega_r)\lambda_{dr} + p\lambda_{qr} = 0$$
$$v_{dr} = R'_r i_{dr} - (\omega - \omega_r)\lambda_{qr} + p\lambda_{dr} = 0 \tag{3}$$

Primary flux linkage equations:

$$\lambda_{qs} = L_{ls} i_{qs} + L_m\{1 - f(Q)\}(i_{qs} + i_{qr})$$
$$\lambda_{ds} = L_{ls} i_{ds} + L_m\{1 - f(Q)\}(i_{ds} + i_{dr}) \tag{4}$$

Secondary flux linkage equations:

$$\lambda_{qr} = L'_{lr} i_{qr} + L_m\{1 - f(Q)\}(i_{qs} + i_{qr})$$
$$\lambda_{dr} = L'_{lr} i_{dr} + L_m\{1 - f(Q)\}(i_{ds} + i_{dr}) \tag{5}$$

where $\omega_r$ denotes the secondary angular speed and $\omega$-$\omega_r$ represents the slip angular frequency ($\omega - \omega_r \equiv \omega_{sl}$).

The thrust developed by the machine can be expressed as:

$$F = \frac{3}{2}\frac{\pi}{\tau}\left(\lambda_{qr} i_{dr} - \lambda_{dr} i_{qr}\right) \tag{6}$$

where $\tau$ denotes the motor pole pitch.

## III. Current and Voltage Limits

Practically, for a motor drive, which is supplied through an inverter and operates over a wide speed range, the feasible operation range is restricted by the following voltage and current inequalities [9], [15]:

$$(i_{qs})^2 + (i_{ds})^2 \le {I_{\max}}^2 \tag{7}$$

$$(v_{qs})^2 + (v_{ds})^2 \le {V_{\max}}^2 \tag{8}$$

where $I_{\max}$ and $V_{\max}$ represent the maximum amplitudes of current and voltage, respectively [15]. The current limit confines the current magnitude not to exceed the circle specified by $I_{\max}$ shown in Fig. 2. Similarly, the voltage constraint restricts the voltage magnitude to the ellipse determined by $V_{\max}$ illustrated in Fig. 2. Consequently, the possible operating region is the common area of the current limit circle and voltage limit ellipse and is dashed in Fig. 2 [15].

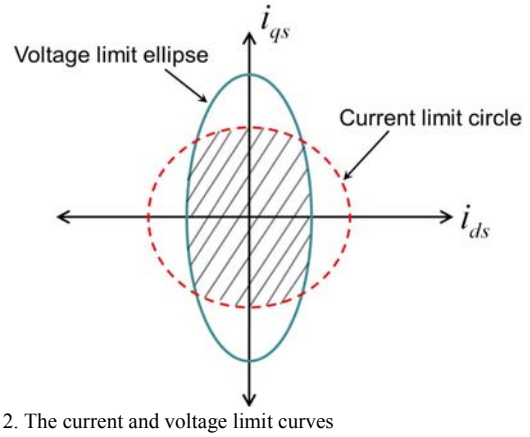


Figure 2. The current and voltage limit curves

In steady-state condition, the primary voltage equations that describe the behavior of the LIM are as follows:

$$v_{qs} = R_s i_{qs} + \omega\lambda_{ds} \tag{9}$$

$$v_{ds} = R_s i_{ds} - \omega\lambda_{qs} \tag{10}$$

In an ideally decoupled LIM, the secondary flux linkage

is forced to align with the d-axis ( $\lambda_{qr} = 0$ ). Therefore, in steady state condition, simplifying (3) follows that:

$$i_{qr} = -i_{qs}\left[\frac{1-f(Q)}{\frac{L'_{lr}}{L_m}+(1-f(Q))}\right] \quad (11)$$

$$i_{dr} = \circ \quad (12)$$

Eliminating $i_{qr}$ and $i_{dr}$ in (4) using (11) and (12) gives:

$$\lambda_{qs} = [L_{ls} + \frac{L'_{lr}(1-f(Q))}{\frac{L'_{lr}}{L_m}+(1-f(Q))}]\times i_{qs} \quad (13)$$

$$\lambda_{ds} = [L_{ls} + L_m(1-f(Q))]\times i_{ds} \quad (14)$$

Substituting (13) and (14) into (9) and (10), respectively, results in:

$$v_{qs} = R_s\, i_{qs} + \omega_e K_1\, i_{ds} \quad (15)$$

$$v_{ds} = R_s\, i_{ds} - \omega_e K_2\, i_{qs} \quad (16)$$

where

$$K_1 = L_{ls} + L_m(1-f(Q)) = L_s$$

$$K_2 = L_{ls} + \frac{L'_{lr}(1-f(Q))}{\frac{L'_{lr}}{L_m}+(1-f(Q))} = \sigma L_s$$

$$\sigma = 1 - \frac{L_m{}^2(1-f(Q))^2}{L_s + L'_r}$$

where σ is the leakage factor.

Consequently, by substituting (15) and (16) in (8), the inequality for the voltage limit ellipse can be derived:

$$(R_s\, i_{qs} + \omega_e K_1\, i_{ds})^2 + (R_s\, i_{ds} - \omega_e K_2\, i_{qs})^2 \le V_{s_{\max}}^2 \quad (17)$$

In higher speeds, the voltage drop due to the primary resistance can be neglected and the voltage limit becomes a simple ellipse centered on the origin:

$$(\omega_e K_1\, i_{ds})^2 + (\omega_e K_2\, i_{qs})^2 \le V_{s_{\max}}^2 \quad (18)$$

When the LIM speed increases, the voltage limit ellipse of (18) will shrink toward the origin.

Due to the end effect consideration in the LIM dynamic model, the $K_1$ and $K_2$ gains depend on the motor speed through $f(Q)$. In Fig. 3 the variation of $f(Q)$ according to the LIM speed is illustrated. In order to neglect the voltage drop of the primary resistance, the terms $\omega_e K_1$ and $\omega_e K_2$ should be compared with $R_s$. Fig. 4 demonstrates the variation of $\omega_e K_1$ and $\omega_e K_2$ according to the LIM speed. It is clear that in high-speed operations the voltage drop of primary resistance can be neglected in comparison with $\omega_e K_1$ and $\omega_e K_2$.

In order to satisfy both current limit and voltage limit, the command current vector must be inside the common area of the current limit circle and the voltage limit ellipse [8-9]. In case of Indirect Field-Oriented Control (IFOC) of the LIM, the developed thrust can be expressed as follows:

$$F = \frac{3}{2}\frac{\pi}{\tau}\frac{L_m{}^2.(1-f(Q))^2}{L'_{lr}+L_m(1-f(Q))}\times i_{qs}^* i_{ds}^* \quad (19)$$

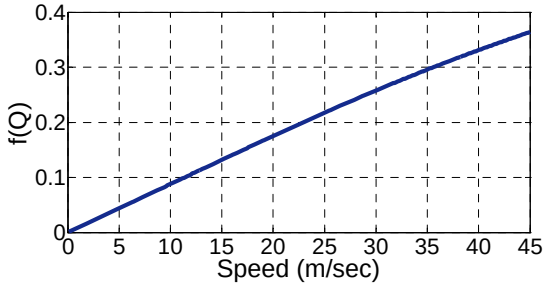


Figure 3. Variation of *f(Q)* according to the LIM speed

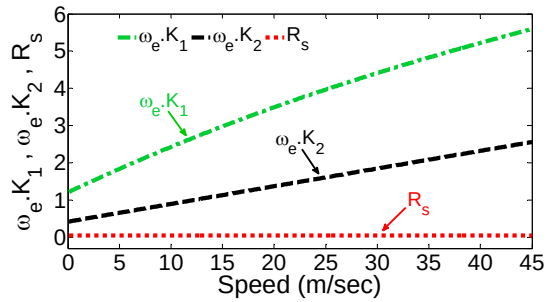


Figure 4. Variation of $\omega_e K_1$ and $\omega_e K_2$ according to the LIM speed

The full operating range of an LIM drive can be divided into the following regions:

- Constant force region ( $\omega_e < \omega_b$ )
- Constant power region or Field-Weakening (FW) region
  - ✓ Partial FW region ( $\omega_b < \omega_e < \omega_c$ )
  - ✓ Full FW region ( $\omega_e \ge \omega_c$ )

In the constant force region, which is below the base angular frequency, $\omega_b$, the LIM force is kept constant. The region above $\omega_b$ is the field-weakening region which can be sub-divided into partial FW region and full FW region. The thrust curve in full operating range of the LIM drive is illustrated in Fig. 5.

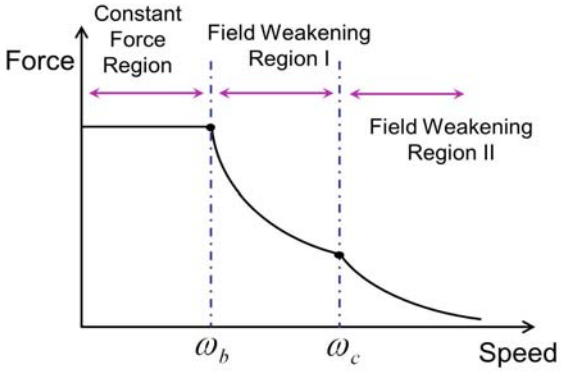


Figure 5. The force curve in full operating range

## IV. Field-Weakening Control Principals With End Effect Consideration

### *A. Constant Force Region ( $\omega_e < \omega_b$ )*

In the constant force region, the desired d-axis primary current, $i_{ds}^*$, which is the crossing point of the ellipse and the circle [15], is smaller than the d-axis primary current for the maximum LIM thrust. In an LIM, the end effect phenomenon leads to the weakening of flux linkage and thrust. The force weakening becomes severe when the speed increases. The LIM force can be expressed as:

$$F = \frac{3}{2}\frac{\pi}{\tau} G(f(Q)) \times i_{ds}^{*} i_{qs}^{*} \quad (20)$$

or

$$F = \frac{3}{2}\frac{\pi}{\tau} H(f(Q)) \times \lambda_{dr}^{*} i_{qs}^{*} \quad (21)$$

where

$$G(f(Q)) = \frac{L_m{}^2.(1-f(Q))^2}{L'_{lr}+L_m(1-f(Q))}$$

$$H(f(Q)) = \frac{L_m.(1-f(Q))}{L'_{lr}+L_m(1-f(Q))}$$

*G(f(Q))* and *H(f(Q))* are functions of *f(Q)* and thus dependent to the LIM speed. In Fig. 6 the variations of *G(f(Q))* and *H(f(Q))* functions are shown according to the LIM speed. It is clear from the figures that *G(f(Q))* is highly dependent to the speed. For example, by increasing the LIM speed from zero to the nominal speed (15 m/s), the *G(f(Q))* function is decreased about 13.342%. Whereas, *H(f(Q))* is less dependent to the speed. For instance, by increasing the LIM speed from zero to the nominal speed (15 m/s), the *H(f(Q))* function is decreased about 0.296%.

Therefore, it is clear from the results that due to the end effects, the LIM force cannot be kept constant even in the constant force region. Consequently, in order to keep the LIM force constant at its optimal value in the constant force region, $i_{ds}^{*}$ cannot be a value and should be properly modified.

Thus, the main objective of this part is to compute proper expressions for $i_{ds}^{*}$ and $i_{qs_{lim}}^{*}$ as functions of *f(Q)*, which results in a constant $F_{max}$, whereas the current limit circle is satisfied:

$$F_{\max} = (\frac{3}{2}\frac{\pi}{\tau}).G(f(Q)) \times i_{ds}^{*}\sqrt{I_{s\max}^2 - i_{ds}^{*\,2}} \quad (22)$$

By considering $i_{ds}^{*}\sqrt{I_{s\max}^2 - i_{ds}^{*\,2}} \times G(f(Q)) = \alpha$ (where $\alpha = F_{max}\frac{2}{3}\frac{\tau}{\pi}$) and after simplifying, the below fourth degree polynomial equation can be obtained:

$$i_{ds}^{*\,4} - I_{s\max}^2 i_{ds}^{*\,2} + \frac{\alpha^2}{G^2(f(Q))} = 0 \quad (23)$$

Solving (23) for $i_{ds}^{*}$ gives the d-axis primary current command as follows:

$$i_{ds}^{*} = \sqrt{\frac{I_{s\max}^2 - \sqrt{I_{s\max}^4 - \frac{4\alpha^2}{G^2(f(Q))}}}{2}} \quad (24)$$

The maximum q-axis current command, $i_{qs_{lim}}^{*}$, can be derived by substituting (24) in the current limit circle:

$$i_{qs\lim}^{*} = \sqrt{\frac{I_{s\max}^2 + \sqrt{I_{s\max}^4 - \frac{4\alpha^4}{G^2(f(Q))}}}{2}} \quad (25)$$

Accordingly, $\lambda_{dr}^{*}$ and $\omega_{sl\_max}$ can be written as follows:

$$\lambda_{dr}^{*} = L_m.(1-f(Q)) \times i_{ds}^{*} \quad (26)$$

$$\omega_{sl\max}(f(Q)) = \omega_{sl}\big|_{F_{\max}} = [\frac{R'_r}{L'_{lr}+L_m(1-f(Q))}] \times \frac{i_{qs\lim}^{*}(f(Q))}{i_{ds}^{*}(f(Q))} \quad (27)$$

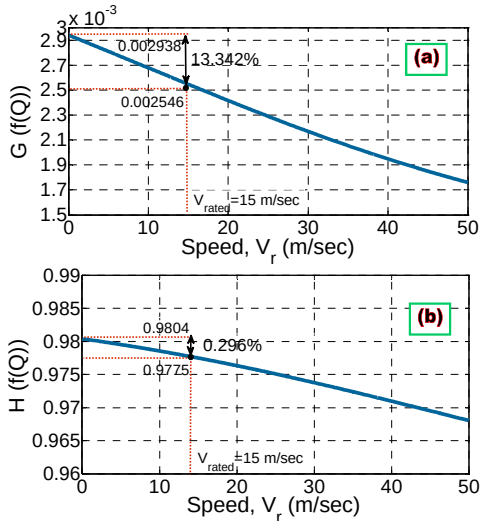


Figure 6. a) *G(f(Q))* as a function of the LIM speed, b) *H(f(Q))* as a function of the LIM speed

In Fig. 7, d-axis current command ($i_{ds}^{*}$), maximum q-axis current command ($i_{qs_{lim}}^{*}$), maximum available force ($F_{max}$), and d-axis secondary flux command ($\lambda_{dr}^{*}$) are represented according to *f(Q)*, respectively.

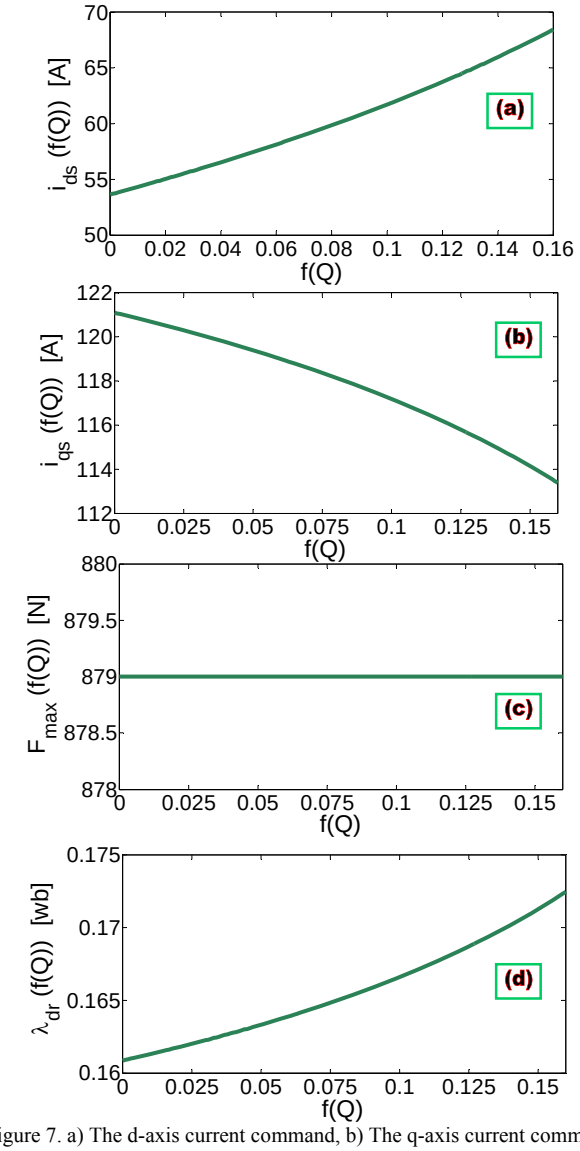


Figure 7. a) The d-axis current command, b) The q-axis current command, c) The maximum available force, d) The d-axis secondary flux command

In the constant force region, the d-axis and q-axis primary current commands totally satisfy the current and voltage constraints [15]. As the operating frequency increases, the size of the voltage limit ellipse reduces [15]. Where the d-axis and q-axis primary current commands of (24) and (25) exceed the voltage limit ellipse, the partial FW region starts [15].

*B. Partial FW Region ( $\omega_b < \omega_e < \omega_c$ )*

The region above $\omega_b$ and below the critical speed, $\omega_c$, is called the partial FW region [15]. The critical speed, $\omega_c$, is the angular speed above which the voltage limit ellipse and the current limit circle have no crossing points [15]. As discussed previously, when the end effect is taken into account, the appropriate current and voltage limit curves can be illustrated as (7) and (18). Like in case of end effect disregard, the d-axis and q-axis current commands that maximize the LIM thrust can be derived from the crossing point of the ellipse and the circle:

$$i_{ds}^{*} = \sqrt{\frac{\left(\frac{V_{s\max}}{\omega_e}\right)^2 - (K_2 I_{s\max})^2}{K_1^{\,2} - K_2^{\,2}}} \tag{28}$$

$$i_{qs\lim}^{*} = \sqrt{I_{s\max}^2 - i_{ds}^{*\,2}} = \sqrt{\frac{(K_1 I_{s\max})^2 - \left(\frac{V_{s\max}}{\omega_e}\right)^2}{K_1^{\,2} - K_2^{\,2}}} \tag{29}$$

The maximum available thrust, which satisfies the current and voltage limits, and the d-axis secondary flux command can be expressed as follows:

$$F_{\max} = \frac{3}{2}\frac{\pi}{\tau} G(f(Q))\, i_{qs\lim}^{*} i_{ds}^{*} \tag{30}$$

$$\lambda_{dr}^{*} = L_m.(1 - f(Q))\, i_{ds}^{*}$$

$$= L_m.(1 - f(Q)) \sqrt{\frac{\left(\frac{V_{s\max}}{\omega_e}\right)^2 - (K_2 I_{s\max})^2}{K_1^{\,2} - K_2^{\,2}}} \tag{31}$$

The maximum available thrust in this region is inversely proportional to the angular speed ( $F_{\max} \propto \frac{1}{\omega_e}$ ).

As depicted in Fig. 8, the base angular frequency, $\omega_b$, can be calculated from the crossing point of $i_{ds}^{*}$, the voltage ellipse, and the current circle [15]:

$$\omega_b = \frac{V_{s\max}}{\sqrt{(K_2 I_{s\max})^2 + \frac{(K_1^{\,2} - K_2^{\,2})}{2} \cdot \left[ I_{s\max}^2 - \sqrt{I_{s\max}^4 - \frac{4\alpha^2}{G^2(f(Q))}} \right]}} \tag{32}$$

It is clear that $\omega_b$ is a function of *f(Q)* and thus dependent to the LIM speed. In Fig. 9 the base angular frequency is demonstrated according to *f(Q)*, in case of neglecting the primary resistance. Since $\omega_b$ is dependent to *f(Q)* and the motor speed, the LIM loading conditions will affect the base angular frequency.

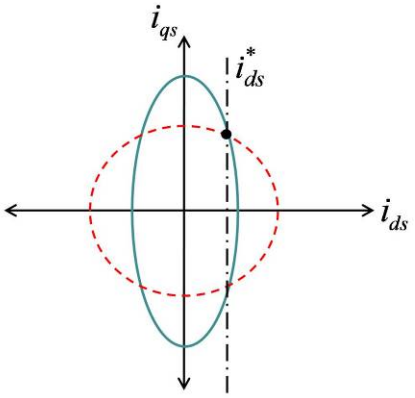


Figure 8. Determination of the base angular frequency

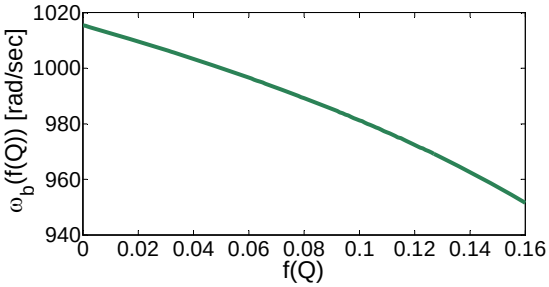


Figure 9. The base angular speed, $\omega_b$, versus f(Q)

*C. Full FW Region ( $\omega_e \geq \omega_c$ )*

Above the critical speed, $\omega_c$, the voltage limit ellipse is totally included in the current limit circle [15], as illustrated in Fig. 10. From now, the voltage ellipse and the current circle have no crossing points [15]. This region is called the full FW region [15].

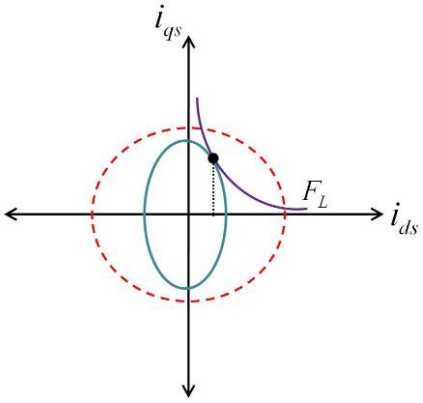


Figure 10. Full field-weakening region (FW-II)

In the full FW region, the LIM thrust is only restricted by the voltage constraint. Consequently, in order to maximize the LIM thrust, only the voltage limit should be satisfied:

$$i_{qs} = \sqrt{\frac{V_{s\,max}^2 - (\omega_e K_1)^2 i_{ds}^2}{(\omega_e K_2)^2}} \tag{33}$$

Since the steady state LIM force is proportional to $i_{ds} \times i_{qs}$, to maximize the force curve, an objective function equal to $i_{ds} \times i_{qs}$ is considered. Then, by substituting (33) in order to satisfy the voltage constraint, the derivative of the objective function with respect to $i_{ds}$ should be calculated and set to zero:

$$F(i_{ds}) = i_{ds} \times i_{qs} = i_{ds} \times \sqrt{\frac{V_{s\max}^2 - (\omega_e K_1)^2 i_{ds}^2}{(\omega_e K_2)^2}} \tag{34}$$

$$\frac{\partial F(i_{ds})}{\partial i_{ds}} = \circ \tag{35}$$

Solving for $i_{ds}$, gives the optimal d-axis and q-axis primary currents as follows:

$$i_{ds}^{*} = \frac{V_{s_{\max}}}{\sqrt{2}\omega_e K_1} = i_{ds-FW\,II}^{*} \tag{36}$$

$$i_{qs\lim}^{*} = \frac{V_{s_{\max}}}{\sqrt{2}\,\omega_e K_2} \tag{37}$$

The maximum available thrust can be expressed as follows:

$$F_{\max} = \frac{3}{2}\frac{\pi}{\tau}\, G(f(Q))\, i_{qs\lim}^{*} i_{ds}^{*} \tag{38}$$

It clear that the maximum LIM thrust is inversely proportional to the square of the angular speed:

$$F_{\max} \propto \frac{1}{\omega_e^2} \tag{39}$$

The critical frequency, $\omega_c$, can be derived from the point where the circle and the ellipse have only one crossing point (as represented in Fig. 11).

$$\omega_c = \left(\frac{V_{s\,\max}}{I_{s\,\max}}\right)\sqrt{\frac{(K_1{}^2 + K_2{}^2)}{2K_1{}^2 K_2{}^2}} \tag{40}$$

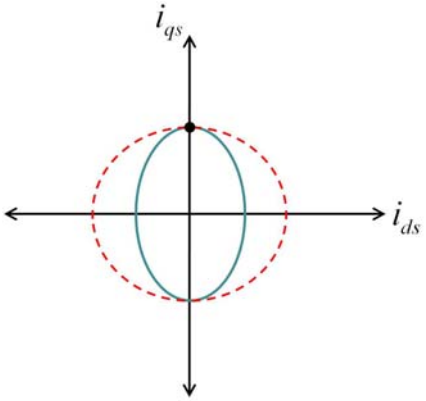


Figure 11. Determination of the critical speed

The slip angular frequency, $\omega_{sl}$, can be derived using (3) and (5) and by eliminating $i_{qr}$ as:

$$\omega_{sl\,\max} = \left[\frac{R_r'}{L'_{lr} + L_m\,(1 - f(Q))}\right] \times \frac{i_{qs\lim}^{*}}{i_{ds}^{*}} \tag{41}$$

The maximum slip frequency, $\omega_{sl\_max}$, can be derived using (36), (37), and (41) as follows:

$$\omega_{sl\,\max} = \left[\frac{R_r'}{L'_{lr} + L_m\,(1 - f(Q))}\right] \left(\frac{K_1}{K_2}\right) \tag{42}$$

It is clear that, when the end effect is considered, $\omega_{sl\_max}$ is not constant and is dependent to the LIM speed.

## V. Control System

The proposed field-weakening IFOC scheme of the LIM drive considering the end effect is demonstrated in Fig. 12 (a). The suggested control structure consists of a current control loop and a speed control loop. In this paper, the fuzzy Logic Controller (FLC) is utilized as a speed regulator. The suggested FW block diagram generates the d-axis primary current command ($i_{ds}^{*}$), the maximum q-axis primary current command ($i_{qs\lim}^{*}$), and the slip frequency ($\omega_{sl}$). The d-axis primary current command, $i_{ds}^{*}$, is generated from the FW block diagram according to the desired d-axis secondary flux, $\lambda_{dr}^{*}$. The speed regulator generates the preliminary q-axis current command using the error between the command speed and the actual speed. Then, after being limited by $i_{qs\lim}^{*}$, the proper q-axis primary current command, $i_{qs}^{*}$, will be produced. Using the inverse Park's transformation, the three-phase primary current commands are produced from the d-axis and q-axis primary current commands [7], [19]. The current regulator compels the LIM current to follow the primary current commands as closely as possible by producing the firing signals of the inverter switches. As a result, the LIM is forced to follow the speed command due to the speed control loop [19]. The d-axis and maximum q-axis primary current commands are determined according to the field-weakening flowchart as represented in Fig. 12 (b).

## VI. Fuzzy Logic Controller (FLC)

Based on the model of linear induction motor, the input and output linguistic variables of the FLC can be determined [20]. The selected input vectors of the FLC are the LIM speed error ($\Delta V_r(n)$) and the change of LIM speed error ($\Delta e(n)$) [20]. For the output vector the command LIM thrust ($F_e^{*}(n)$) is considered. Accordingly, the preliminary command q-axis primary current ($i_{qs}^{*}$) will be produced using (20). The complete block diagram of the suggested FLC for LIM drive incorporating FW control strategy is shown in Fig. 13. After choosing the linguistic variables, the scaling factors $K_\omega$, $K_e$, and $K_i$ for fuzzification should be determined in order to generate the accurate command thrust [20]. The factors $K_\omega$ and $K_e$ should be adjusted in order to normalize $\Delta V_r(n)$ and $\Delta e(n)$ within the limit $\pm 1$ [20]. In this work, these factors are adjusted by trial and error to achieve optimal LIM drive performance according to the simulation results.

In addition, the Mamdani fuzzy inference method has been applied in this work and for defuzzification the center of gravity technique has been used. Moreover, the fuzzy rules for the FLC are obtained from [20] and are as follows:

If $\Delta V_n$ is PH (Positive High), then $F_e^{*}$ is PH.

If $\Delta V_n$ is PL (Positive Low), then $F_e^{*}$ is PM (Positive Medium).

If $\Delta V_n$ is ZE (Zero) and $\Delta e$ is PO (Positive), then $F_e^{*}$ is PL.

If $\Delta V_n$ is ZE and $\Delta e$ is NE (Negative), then $F_e^{*}$ is NC (No Change).

If $\Delta V_n$ is ZE and $\Delta e$ is ZE, then $F_e^{*}$ is NC.

If $\Delta V_n$ is NL (Negative Low), then $F_e^{*}$ is NL.

If $\Delta V_n$ is NH (Negative High), then $F_e^{*}$ is NH.

The applied membership functions for fuzzy sets are demonstrated in Fig. 13 (b).

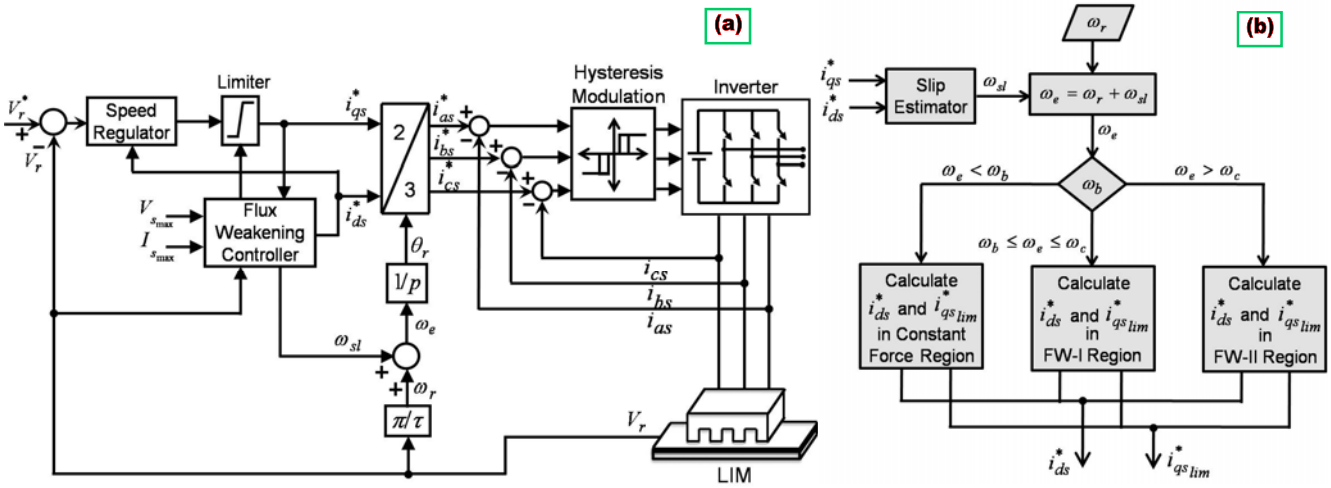


Figure 12. a) Block diagram of the proposed field-weakening IFOC for LIM drive, b) Flowchart of the field-weakening algorithm

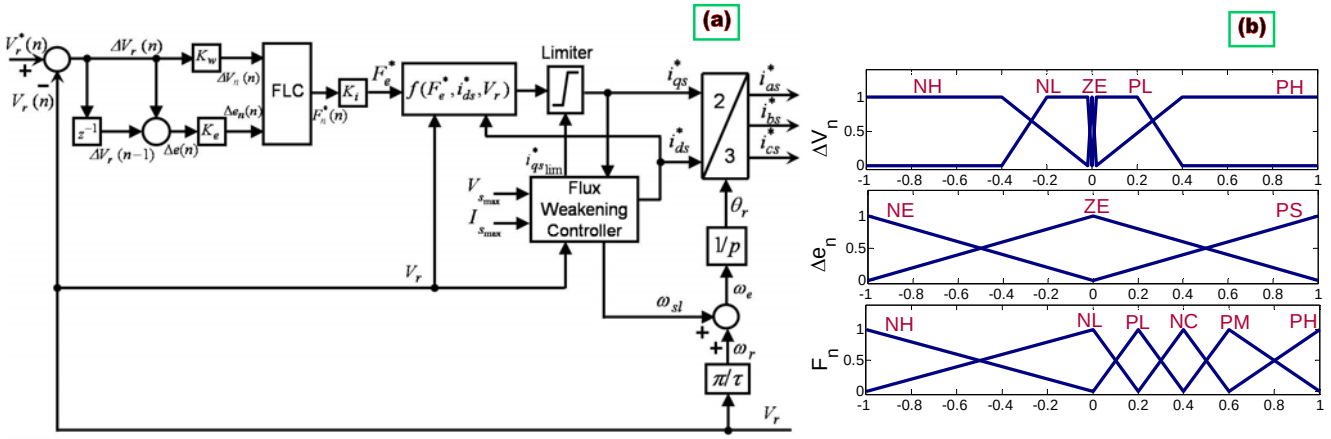


Figure 13. a) Block diagram of the proposed Fuzzy Logic Controller (FLC) of LIM drive with field-weakening strategy, b) Fuzzy logic membership functions; speed error $\Delta V_n$, speed error change $\Delta e_n$, q-axis primary current $F_{en}^*(n)$

## VII. Simulation Results

In order to validate the performance of the suggested fuzzy logic controller based LIM drive including FW control, various tests have been carried out at different operating conditions. The end effect has been taken into account in both LIM model and field-weakening algorithm. The simulation of the complete drive has been performed using Matlab/Simulink software for the prototype LIM of Appendix A. The utilized gains for the fuzzy logic controller are given in Appendix A. Some of the simulated results are presented in the following.

The external force versus speed characteristics with end effect consideration is extracted and is represented in Fig. 14.

In order to consider the end effect in the FW controlling algorithm two patterns have been suggested and evaluated in this paper. These two patterns are represented in Figs. 15 and 16, respectively. In the first pattern, that is shown in Fig. 15, the d-axis flux linkage command, $\lambda_{dr}^*$, is kept constant and thus the LIM force cannot be kept constant even in the constant force region. The LIM force will decrease if the speed (or *f(Q)*) increases. In Fig. 15 (a)-(d) the d-axis current command ($i_{ds}^*$), maximum q-axis current command ($i_{qs_{lim}}^*$), maximum slip frequency ($\omega_{sl\_max}$), and maximum force capability, $F_{L\_max}$ are depicted in the whole field-weakening region of the LIM drive. Furthermore, in order to consider the end effect, a third dimension according to *f(Q)* has been taken into account and the curves are plotted with three dimensions.

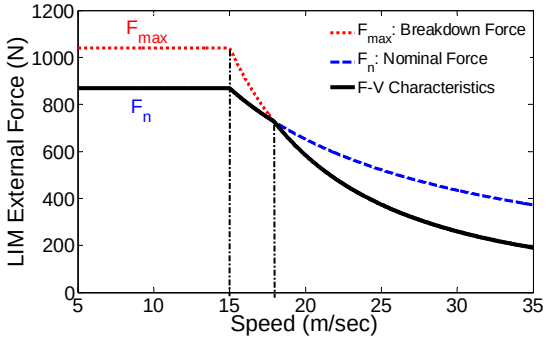


Figure 14. Force versus speed characteristics with end effects

In the second pattern, in order to keep the LIM force constant in the constant force region, the command d-axis and q-axis currents should be properly modified using (24) and (25), respectively. In Fig. 16 (a)-(d) the d-axis current command ($i_{ds}^*$), maximum q-axis current command ($i_{qs_{lim}}^*$), maximum slip frequency ($\omega_{sl\_max}$), and maximum force capability ($F_{L\_max}$) are illustrated according to the proposed

strategy. The reference speed is changed in step shape from 15 m/sec (the rated speed) to 25 m/sec at t=1 sec. At t=4 sec, the reference speed is further increased to 35 m/sec and at t=7 sec decreased to 20 m/sec. At first, the LIM is driven at no load condition. At t=2 sec a step load force 340 N is applied to the LIM and at t=3 sec the load is removed. At t=6 sec a 185 N load force is applied which is further increased to 385 N at t=8 sec. It can be clearly seen from these figures that the actual speed tracks the reference speed precisely and the transitions between the constant torque and FW conditions are smooth and with no overshoot. The controller incorporating field-weakening control offers excellent speed response and performance.

The phase 'a' current and phase 'a' voltage of the LIM drive are represented in Figs. 17 (b)-(c). As shown in the figures, both current and voltage waveforms never exceed from their maximum values $I_{s\ max}$ and $V_{s\ max}$, respectively, which in turn validates the accurate performance of the FW control strategy for LIM drive. In Figs. 17 (d)-(e) the current limit curve ($i_{ds}^2+i_{qs}^2$) and the voltage limit curve ($v_{ds}^2+v_{qs}^2$) are shown. It is clear from the results that both current limit and voltage limit never exceed from their maximum values $I_{s\ max}$ and $V_{s\ max}$, respectively. The parts in which the current limit waveform is restricted to $I_{s\ max}$ are in accordance with the partial field-weakening region. Moreover, the parts in which the voltage limit waveform is restricted to $V_{s\ max}$ are in accordance with the full field-weakening region. Fig. 17 (f) demonstrates the electrical angular speed $\omega_e$ in compare with the base speed $\omega_b$ and the critical speed $\omega_c$. The sections, in which the angular speed $\omega_e$ is below the base speed, are related to the constant force region. The sections, in which the angular speed $\omega_e$ is above the base speed and below the critical speed, are related to the partial field-weakening region. In addition, the parts, in which the angular speed $\omega_e$ exceed from the critical speed, are in accordance with the full field-weakening region. Moreover, as can be seen in this figure, due to the end effect the base speed $\omega_b$ and the critical speed $\omega_c$ are not constant and vary with angular speed $\omega_e$.

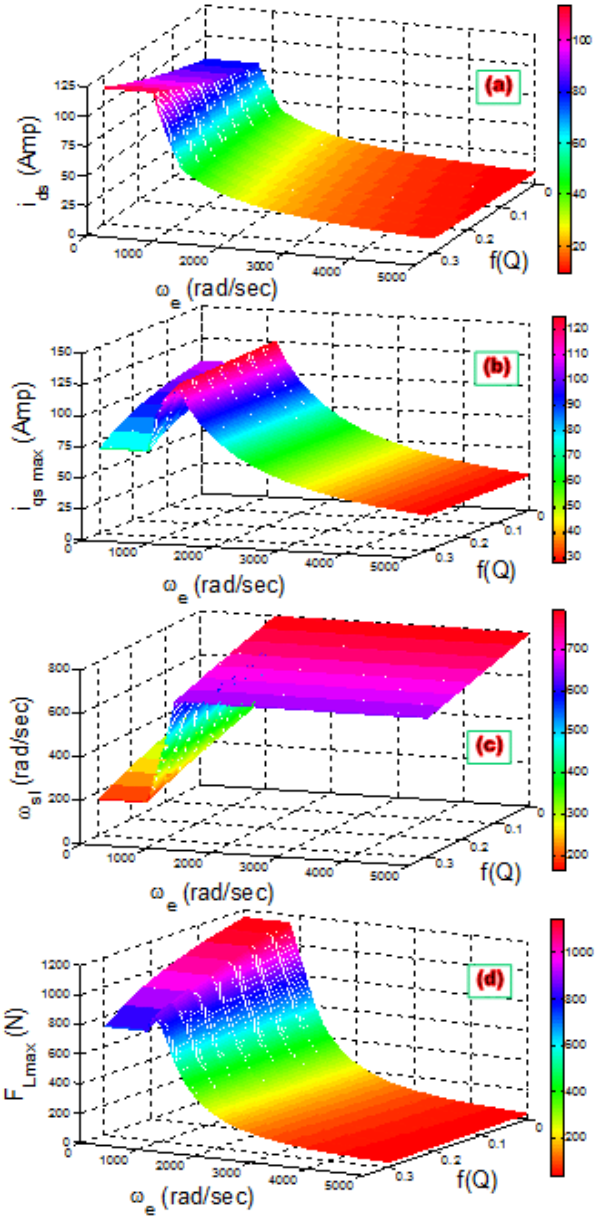


Figure 15. First FW method: a) d-axis current command, b) Maximum q-axis current command, c) Maximum slip frequency, d) Maximum force capability versus speed with end effects

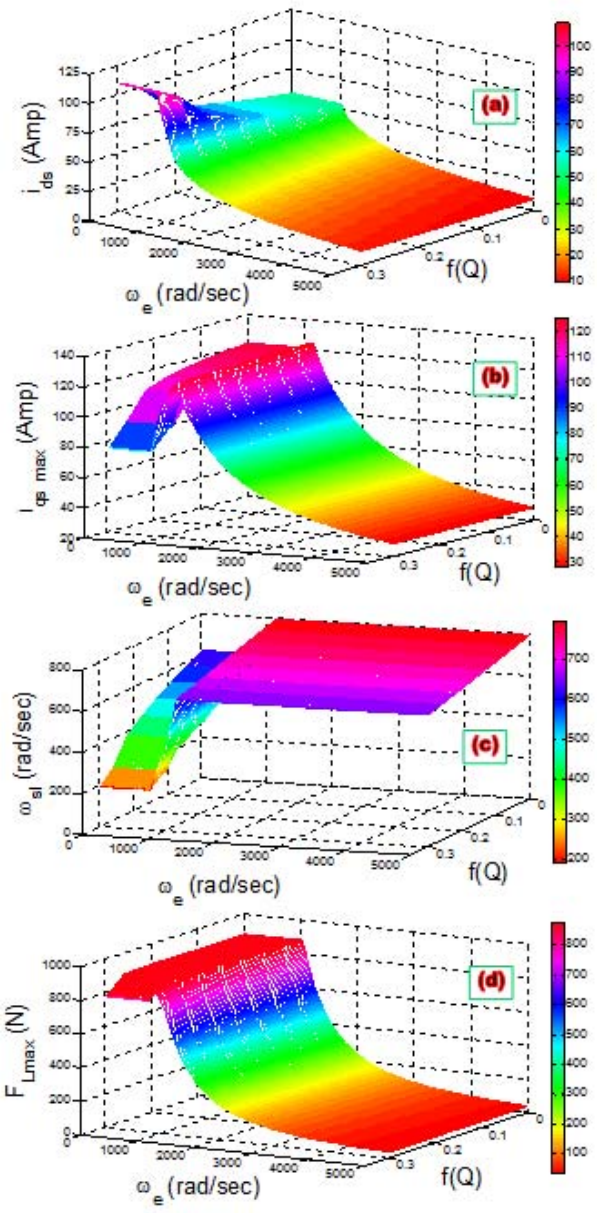


Figure 16. Second FW method: a) d-axis current command, b) Maximum q-axis current command, c) Maximum slip frequency, d) Maximum force capability versus speed with end effects

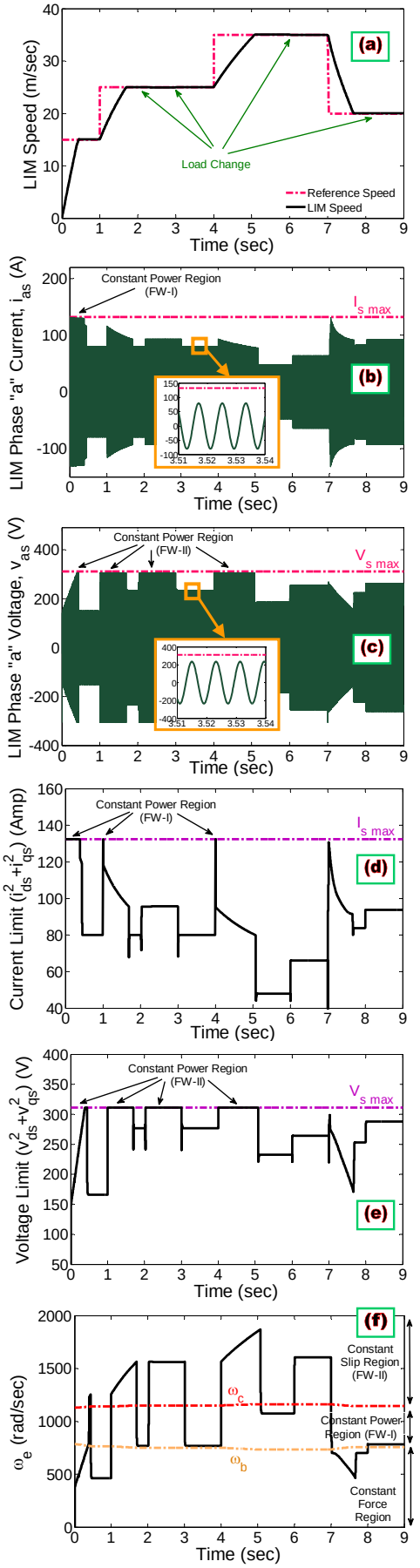


Figure 17. First FW method: a) Speed response, b) The phase 'a' current of the LIM, c) The phase 'a' voltage of the LIM, d) Current limit, e) Voltage limit, f) Electrical angular frequency with end effects

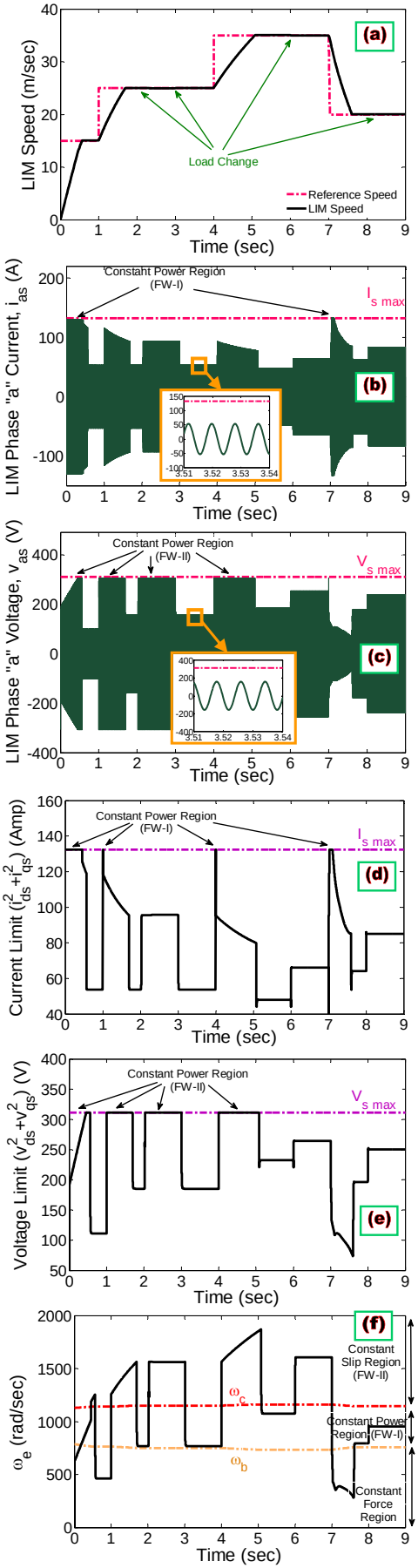


Figure 18. Second FW method: a) Speed response, b) The phase 'a' current of the LIM, c) The phase 'a' voltage of the LIM, d) Current limit, e) Voltage limit, f) Electrical angular frequency with end effects

On the other hand, the above tests are repeated for the second pattern of Fig. 16 (i.e. proposed constant force strategy) and the results are represented in Fig. 18. The command speed and the loading conditions are the same as

Fig. 17. By comparing the results of Figs. 17 and 18, it is clear that in both methods the LIM speed tracks the reference speed under different loading conditions and in both motoring mode and breaking mode. Both speed responses have fast dynamic with no overshoot and negligible steady state error and are adaptive to force changes and speed changes. As can be seen from the figures, the second constant force pattern in comparison with the first pattern leads to remarkably lower current and voltage amplitudes in both constant force and partial field-weakening regions. However, in the full field-weakening region, both patterns yield similar results because they use the same d-axis and q-axis current commands.

## VIII. CONCLUSION

Due to the lack of adequate researches on field-weakening control of linear machines, this paper concentrates on the field-weakening control of Linear Induction Motors (LIMs) considering the end effect. New voltage and current limits are analytically calculated for LIM drives considering the end effect. Accordingly, new control strategies such as constant force region, partial field-weakening region, and full field-weakening region are extracted for LIM drives using the new calculated voltage and current limits considering the end effect. In addition, fuzzy logic controller has been properly applied to enhance the dynamic performance of the LIM drive. Simulation results confirm that the recommended fuzzy logic LIM drive with the flux control technique offers excellent features such as fast response, no overshoot, low steady-state error, and adaptability to load changes. Therefore it is appropriate for high-performance drive applications. Moreover, the new constant force pattern suggested in this paper moderates the weakening of the LIM thrust due to the end effect and results in lower current and voltage amplitudes in both constant force and partial field-weakening regions.

## APPENDIX A

Fuzzy Logic controller gains: $K_\omega$=0.0257,$K_e$=1.5,$K_i$=1813

LIM PARAMETERS

| | | | | | |
|---|---|---|---|---|---|
| Phase voltage | 220 V | Secondary length | 0.413 m | $L_m$ | 3 mH |
| Current | 93.65 A | $R_s$ | 0.049 Ω | $\lambda^*_{dr}$ | 0.24 Wb |
| Power factor | 0.4884 | $R'_r$ | 0.803 Ω | $M$ | 29.34 kg |
| Pole pairs | 2 | $L_{ls}$ | 1.5 mH | slip | 0.5 |
| Pole pitch | 0.1024 m | $L'_{lr}$ | 4% $L_{ls}$ | Rated force | 879 N |

## REFERENCES


[1] J. Duncan and, C. Eng, "Linear induction motor-equivalent-circuit model," IEE Proc. Power Application , Vol. 130, No. 1, pp. 51-57, Jan. 1983. doi:10.1049/ip-b.1983.0008

[2] K. Nam, J. H. Sung, "A new approach to vector control for linear induction motor considering end effects," in Proc. Of the IEEE Industry Applications Conference, Vol. 4, pp. 2284-2289, Oct. 1999. doi:10.1109/IAS.1999.799162

[3] B. Susluoglu, V. M. Karsli, "Direct thrust controlled linear induction motor including end effect," in Proc. of the 13th International Power Electronics and Motion Control Conference (EPE-PEMC), pp. 850-854, Sept. 2008. doi:10.1109/EPEPEMC.2008.4635373

[4] J. Zhao, Z. Yang, J. Liu, T. Q. Zheng, "Indirect vector control scheme for linear induction motors using single neuron PI controllers with and without the end effects," in Proc. of the 7th Word Congress on Intelligent Control and Automation, pp. 5263-5267, China, June 2008. doi:10.1109/WCICA.2008.4593785

[5] E. F. Silva, E. B. Santos, P. C. M. Machado, M. A. A. Oliveira, "Vector control for linear induction motor," 3rd IEEE International Conference on Industrial Technology (ICIT 2003), pp. 518-523, Maribor, Slovenia, Dec. 2003. doi:10.1109/ICIT.2003.1290384

[6] G. Kang and, K. Nam, "Field-oriented control scheme for linear induction motor with the end effect," IEE Proc. on Electric Power Appl., Vol. 152, No. 1, pp. 1565-1572, Nov. 2005. doi:10.1049/ip-epa:20045185

[7] P. Hamedani, A. Shoulaie, J. M. M. Sadeghi, "Cascaded H-Bridge inverters with multiband hysteresis modulation for vector control of multiphase linear induction motor drives considering the end effects, " in Proc. of the 3rd International Conference on Recent Advances in Railway Engineering (ICRARE-2013), Tehran, Iran, May. 2013.

[8] S. H. Kim, S. K. Sul, "Maximum torque control of an induction machine in the field weakening region," IEEE Transactions on Industry Applications, Vol. 31, No. 4, pp. 787-794, 1995. doi:10.1109/IAS.1993.298955

[9] S. H. Kim, S. K. Sul, "Voltage control strategy for maximum torque operation of an induction machine in the field-weakening region," IEEE Transaction on Industrial Electronics, vol. 44, no. 4, pp. 512-518, Aug. 1997. doi:10.1109/41.605628

[10] E. Levi, M. Wang, "A speed estimator for high performance sensorless control of induction motors in the field weakening region," IEEE Transaction on Power Electronics, vol. 17, no. 3, pp. 365-378, May. 2002. doi:10.1109/TPEL.2002.1004244

[11] J. K. Seok, S. K. Sul, "Optimal flux selection of an induction machine for maximum torque operation in flux-weakening region," IEEE Transaction on Power Electronics, vol. 14, no. 4, pp. 700-708, July 1999. doi:10.1109/63.774208

[12] S. H. Song, J. W. Choi, S. K. Sul, "Transient torque maximizing strategy of induction machine in field weakening region," IEEE Power Electronics Specialists Conference (PESC), vol. 2, pp. 1569-1574, Fukuoka, May 1998. doi:10.1109/PESC.1998.703387

[13] K. Nguyen-Thac, T. Orlowska-Kowalska, G. Tarchala, "Comparative analysis of the chosen field-weakening methods for the direct rotor flux oriented control drive system," Archives of Electrical Engineering, vol. 61, no. 4, pp. 443-454, 2012. doi:10.2478/v10171-012-0038-7

[14] K. Nguyen-Thac, T. Orlowska-Kowalska, G. Tarchala, "Influence of the stator winding resistance on the field-weakening operation of the DRFOC induction motor drive," Bulletin of the Polish Academy of Sciences –Technical Sciences, vol. 60, no. 4, pp. 815-823, 2012. doi:10.2478/v10175-012-0095-5

[15] S. K. Sul, "Control of Electric Machine Drive Systems," Wiley-IEEE Press, Feb. 2011.

[16] G. G. Lopez, F. S. Gunawan, J. E. Walters, "Current control of induction machines in the field-weakened region," IEEE Transactions on Industry Applications, vol. 43, no. 4, pp. 981-989, 2007. doi:10.1109/TIA.2007.900459

[17] X. Xu, D. W. Novotny, "Selection of the flux reference for induction machine drives in the field weakened region," IEEE Transactions on Industry Applications, vol. 28, no. 6, pp. 1353-1358, 1992. doi:10.1109/28.175288

[18] A. Shiri, A., Shoulaie, "End effect braking force reduction in high-speed single-sided linear induction machine," International Journal of Energy Conversion and Management, Elsevier, Vol. 61, pp. 43-50, 2012. doi:10.1016/j.enconman.2011.11.014

[19] P. Hamedani, A. Shoulaie, "Indirect field oriented control of linear induction motors considering the end effects supplied from a cascaded H-bridge inverter with multiband hysteresis modulation," in Proc. of the 4th Power Electronics Drive Systems and Technologies Conference (PEDSTC), pp. 13-19, Tehran, Iran, Feb. 2013. doi:10.1109/PEDSTC.2013.6506665

[20] B. Mirzaeian, A., Kiyoumarsi, P. Hamedani, C. Lucas, "A new comparative study of various intelligent based controllers for speed control of IPMSM drives in the field-weakening region," International Journal of Expert Systems with Applications, Elsevier, Vol. 38, Issue. 10, pp. 12643-12653, Sept 2011. doi:10.1016/j.eswa.2011.04.052